PHYSICAL REVIEW B **105**, 085409 (2022)

Second-harmonic generation in atomically thin 1*T*-TiSe$_2$ and its possible origin from charge density wave transitions

Ruiming Zhang,[1] Wei Ruan,[1] Junyao Yu,[1] Libo Gao,[1,2] Helmuth Berger,[3] László Forró,[3] Kenji Watanabe,[4] Takashi Taniguchi,[5] Ahmad Ranjbar,[6] Rodion V. Belosludov,[7] Thomas D. Kühne,[6] Mohammad Saeed Bahramy,[8,*] and Xiaoxiang Xi[1,2,†]

[1]*National Laboratory of Solid State Microstructures and Department of Physics, Nanjing University, Nanjing 210093, China*
[2]*Collaborative Innovation Center of Advanced Microstructures, Nanjing University, Nanjing 210093, China*
[3]*Institute of Condensed Matter Physics, École Polytechnique Fédérale de Lausanne, 1015 Lausanne, Switzerland*
[4]*Research Center for Functional Materials, National Institute for Materials Science, 1-1 Namiki, Tsukuba 305-0044, Japan*
[5]*International Center for Materials Nanoarchitectonics, National Institute for Materials Science, 1-1 Namiki, Tsukuba 305-0044, Japan*
[6]*Dynamics of Condensed Matter and Center for Sustainable Systems Design, Theoretical Chemistry, University of Paderborn, Paderborn 33098, Germany*
[7]*Institute for Materials Research, Tohoku University, Sendai 980-8577, Japan*
[8]*Department of Physics and Astronomy, The University of Manchester, Oxford Road, Manchester M13 9PL, United Kingdom*

(Received 17 November 2021; revised 31 January 2022; accepted 1 February 2022; published 8 February 2022)

Optical second-harmonic generation (SHG) can only occur in noncentrosymmetric crystals in the leading electric-dipole approximation. Transition metal dichalcogenides with the 1*T* octahedral coordination is centrosymmetric, hence precluding SHG. Here we report the surprising observation of SHG in atomically thin 1*T*-TiSe$_2$, a prototypical charge density wave (CDW) material. Its intensity peaks in the trilayer, reaching 2% of that in monolayer MoS$_2$, a two-dimensional crystal featuring pronounced nonlinear optical effect. The SHG signal exhibits a sixfold polarization dependence characteristic of a lattice with threefold rotational symmetry. It monotonically decreases with increasing temperature and persists at room temperature. Raman spectroscopy demonstrates that the CDW order is robust in atomically thin samples, with the transition temperature slightly lower than in the bulk. The SHG can be explained by the lattice distortion associated with the CDW as well as its fluctuation above the transition temperature. These results challenge the exciton insulator scenario and the chiral nature of the CDW, but support the band Jahn-Teller mechanism. Our work demonstrates SHG as a sensitive probe of the stacking order of the CDW in 1*T*-TiSe$_2$ and enriches the material base for nonlinear optical effects.

DOI: 10.1103/PhysRevB.105.085409

I. INTRODUCTION

Monolayer two-dimensional (2D) materials exhibit rich electronic properties owing to the enhanced quantum effect in confined dimensions and their susceptibility to external stimuli. The stacking of monolayers can dramatically modify their electronic properties, as highlighted by the recent development in 2D correlated electronic phases. For instance, interlayer tunneling is the key to engineering the flat band in magic-angle twisted bilayer graphene [1,2], which harbors correlated insulating states and unconventional superconductivity. In another example, both CrI$_3$ and CrBr$_3$ order ferromagnetically in their monolayer form, but their bilayers are antiferromagnetic and ferromagnetic, respectively, governed by the stacking-dependent exchange coupling [3,4]. Charge density wave (CDW) is another type of quantum state commonly found in 2D metals [5], exhibiting simultaneous periodic charge modulation and lattice distortion. While 2D CDW has been shown ubiquitous [5], the role of stacking order on the CDW ground state remains poorly understood [6,7].

1*T*-TiSe$_2$ (referred to as TiSe$_2$ hereafter) is a canonical CDW material, featuring a commensurate transition at approximately 200 K into a $2a_0 \times 2a_0 \times 2c_0$ distorted lattice [8]. The CDW involves atomic displacement associated with wave vectors connecting the Γ point and the three equivalent *L* points in the reciprocal space, superimposed to form a triple-*q* state [8]. The mechanism of the CDW remains controversial and lively discussed [8–19]. With Cu intercalation [20], pressure tuning [21], or electron doping [22], the CDW phase is suppressed and a superconducting dome emerges, offering a rare platform to explore the interplay between these phases. Recently, atomically thin TiSe$_2$ has been produced using a variety of methods [23–33], consistently showing CDW but with disparate thickness dependence of the transition temperature. Chiral superconductivity was predicted to occur in monolayer TiSe$_2$ after quenching a possible imaginary CDW order [34]. Intriguingly, experimental evidence suggests that the CDW phase is also chiral [35–37], which involves helical stacking of the CDW components, instead of the typical stacking of 2D CDW layers. This view was, however, challenged by later works [38–41]. Although transient reflectivity initially lent

---

[*] m.saeed.bahramy@manchester.ac.uk
[†] xxi@nju.edu.cn

2469-9950/2022/105(8)/085409(9)

credence to the twofold rotational symmetry characteristic of the chiral CDW state [35], no further evidence has been reported to confirm such a symmetry. Moreover, since the chiral CDW rests upon the $2c_0$ periodicity along the stacking direction, it remains unknown whether the stacking order is retained in the 2D limit to support this phase.

Optical second-harmonic generation (SHG) has been proven effective to characterize the crystal symmetry and the interlayer stacking in 2D materials. A prime example is the trigonal-prismatic transition metal dichalcogenides, for which SHG establishes distinct layer-number dependencies for the 2*H*- and 3*R*-type stacking [42–46]. The lattice symmetry is encoded in the second-order nonlinear susceptibility $\chi^{(2)}$, enabling the determination of the crystal orientation [42–45]. The SHG technique also provides a sensitive probe of phase transitions in 2D, such as the antiferromagnetic order in bilayer CrI_3 [47] and the ferroelectric order in atomically thin $\mathrm{In}_2\mathrm{Se}_3$ [48,49]. As we show in this work, the CDW-related lattice distortion in TiSe_2 makes it possible to probe the symmetry and the stacking order of its CDW phase.

Here we report a combination of Raman scattering and SHG study on TiSe_2 from bulk down to bilayer, the thinnest obtained in this work. The samples are well protected by encapsulation, enabling us to investigate their intrinsic properties, which sets this work apart from prior reports on samples prone to degradation [23,24]. The Raman data show the CDW amplitude mode from bulk down to bilayer, demonstrating the persistence of the CDW order in atomically thin TiSe_2. The CDW transition temperature (T_{CDW}) is found to weakly depend on the sample thickness, only slightly suppressed in the 2D limit. SHG is observed in samples of all thickness and reaches a maximum in the trilayer. Furthermore, it decreases monotonically with increasing temperature and persists above T_{CDW}. Employing first-principles calculations, we will reconcile the observation of SHG in this otherwise centrosymmetric crystal with the characteristics of the CDW-related lattice distortion as well as its fluctuation up to room temperature.

II. RAMAN CHARACTERIZATION OF CDW TRANSITIONS

Figure 1(a) shows a schematic for the TiSe_6 octahedron, which is centrosymmetric with the Ti atom as the inversion center. Such octahedra form the monolayer TiSe_2 by edge sharing, as shown in Fig. 1(b), and bulk TiSe_2 consists of the monolayers vertically stacked by van der Waals forces. Figure 1(c) shows the low-frequency Stokes and anti-Stokes Raman modes in few-layer TiSe_2. Two sets of peaks can be identified, both blue shifting upon reducing the layer number. These have been previously assigned as the interlayer shear modes [24]. The peak positions are shown in Fig. 1(d), with the lower branch following the form $[1-\cos(\pi/N)]^{1/2}$, where N is the layer number. For thicker samples we rely on atomic force microscopy to determine their thickness. Apart from these low-frequency modes, the crystal lattice features two Raman-active phonon modes with E_g and A_{1g} symmetry [50] [see Fig. 1(e)]. These are associated with the in-plane and out-of-plane vibrations of the Se atoms in the unit cell.

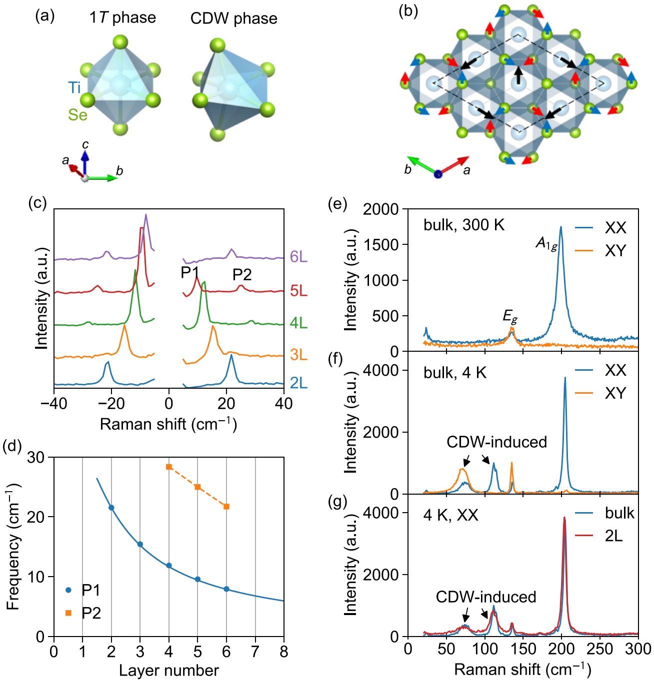

FIG. 1. (a) Exaggerated illustration of octahedral coordination of TiSe_2 in 1*T* and CDW phases for the topmost TiSe_6 octahedron in (b). (b) 2 × 2 lattice reconstruction in the CDW phase in a monolayer unit. The arrows represent directions of the atomic displacement with respect to the pristine lattice, with the blue and red colors for the Se atoms in the plane above and below the Ti plane, respectively. (c) Low-frequency Raman spectra of few-layer TiSe_2 measured at 300 K in the cross polarization configuration. The peak positions are shown in (d). The solid line is a fit to $[1-\cos(\pi/N)]^{1/2}$. (e)–(g) The E_g and A_{1g} phonon modes and the CDW-induced modes in bulk and bilayer TiSe_2. XX and XY denote data collected in the collinear and cross polarization configurations, respectively.

When the CDW transition sets in, a fraction of Ti and Se atoms experience in-plane displacement, forming a superlattice. The commonly accepted superlattice pattern is illustrated in Fig. 1(b) [8]. The space group D_{3d}^3 for the high-temperature phase changes to D_{3d}^4 [50]. Clear CDW-induced Raman modes are observed in both bulk and bilayer samples [see Figs. 1(f) and 1(g)]. These are the characteristic CDW amplitude modes [51–53], attributed to the collective excitations associated with the amplitude of the complex order parameter. Their observation immediately proves the persistence of the CDW phase in atomically thin TiSe_2. Figure 1(g) shows that on the one hand the bilayer A_{1g} mode has a linewidth comparable to that of the bulk, indicating the absence of degradation-induced broadening; on the other hand the amplitude modes in the bilayer are significantly broader, suggesting a less coherent CDW phase.

We carried out a comprehensive temperature- and thickness-dependent Raman characterization of the CDW transition. Figures 2(a)–2(c) are the intensity maps for bulk, trilayer, and bilayer samples. The most pronounced feature is the amplitude mode slightly below 80 cm^{-1}. The mode is weaker in the trilayer than in the bulk, but appears to be enhanced in the bilayer. Note that the large background in

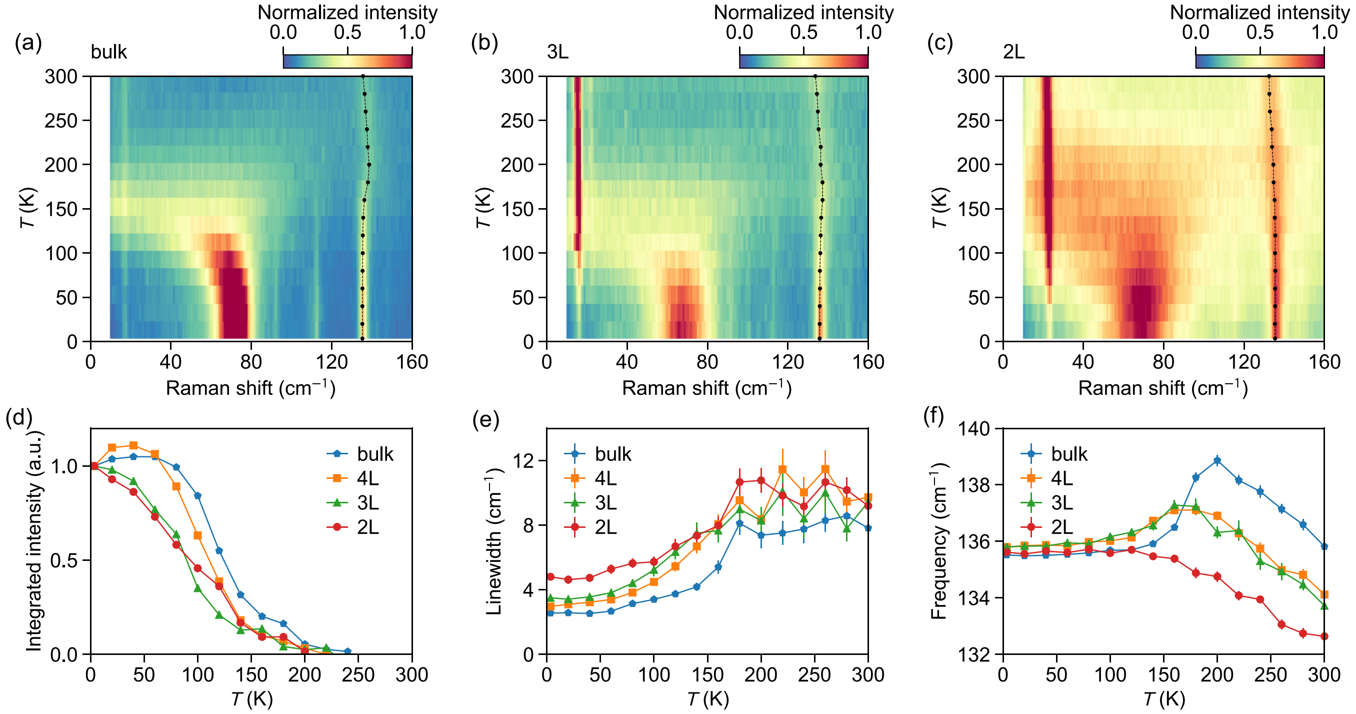

FIG. 2. (a)–(c) Temperature-dependent Raman scattering intensity maps for bulk, trilayer, and bilayer $TiSe_2$ measured in the cross polarization configuration. The intensities have been normalized to that of the corresponding maximum of the CDW amplitude mode. (d) Temperature dependence of the integrated intensity for the amplitude mode, normalized to the value at 4 K. (e),(f) Temperature dependence of the linewidth and frequency of the E_g phonon. The latter is also overlaid on (a)–(c). Error bars are standard deviations from the peak fitting.

Fig. 2(c) gives a false impression of the enhanced amplitude mode. By integrating the mode with respect to a linear background (see Supplemental Material Fig. S1 [54]), we obtain its temperature dependence, shown in Fig. 2(d). The mode is overdamped just below the transition, causing the long tail in the temperature dependence shown in Fig. 2(d), so that accurate determination of T_{CDW} is challenging. Nevertheless T_{CDW} appears weakly dependent on thickness and slightly suppressed (by less than 20 K) in atomically thin samples.

The weak thickness dependence of T_{CDW} is also supported by the linewidth of the E_g phonon mode. Figure 2(e) shows that irrespective of the sample thickness, upon cooling, the linewidth first remains almost unchanged and then monotonically decreases below 180 K. This correlates well with the temperature dependence of the electronic scattering rate in bulk $TiSe_2$ [13]. It was shown that the CDW transition is accompanied by partial gapping of the Fermi surface and reduction of the carrier density. These cause the sharp suppression of electronic scattering and the concomitant increase of the phonon lifetime due to the reduced electron-phonon coupling, hence the reduction of the phonon linewidth below T_{CDW}. The inflection point at approximately 180 K in Fig. 2(e) therefore signifies the CDW transition. Previous work used the maximum in the E_g mode frequency as a criterion to determine T_{CDW} [24]. It works for the bulk sample, but fails for the bilayer because no clear maximum exists [see Fig. 2(f)]. The E_g mode frequency exhibits a peculiar dichotomy between its thickness-dependent temperature dependence and its highly consistent value deep in the CDW phase. This suggests that the formation of CDW significantly weakens the interlayer coupling that gives rise to thickness-dependent E_g mode frequency above T_{CDW}. This picture is also supported by the weakened shear mode intensity upon entering the CDW phase, clearly shown by the data in Figs. 2(b) and 2(c).

III. OBSERVATION AND CHARACTERIZATION OF SHG

We now turn to the most important finding of this work—the observation of SHG in $TiSe_2$. Figure 3(a) shows the spectrum of the fundamental excitation as well as of the SHG. The 1:2 energy ratio verifies the SHG process. Figure 3(b) shows that the SHG intensity scales quadratically with the fundamental power, in excellent agreement with expectation. The sixfold polarization dependence shown in Fig. 3(c) indicates a threefold rotation symmery of the underlying lattice. Fiure 3(d) compares the SHG signal from $2H$-MoS_2 and $TiSe_2$ of different thickness, measured under the same conditions (sample on sapphire substrate, incident power of 2 mW, integration time of 1 s, 4 K, polarization selected to maximize SHG). Although the SHG in the trilayer $TiSe_2$ is only about 2% of that of monolayer MoS_2, this is remarkably strong, considering that monolayer MoS_2 is among the best 2D crystals exhibiting nonlinear optical effects, and that the intensity of trilayer $TiSe_2$ is 20 times greater than that of the centrosymmetric bilayer $2H$-MoS_2. We further note that the SHG is highly sensitive to sample quality. We observed degradation caused by illumination of ultrafast laser pulses on an unprotected trilayer sample (see Supplemental Material Note 1 [54]). A less coherent CDW state with T_{CDW} reduced by about 20 K is accompanied by a 25-fold suppression of the SHG intensity.

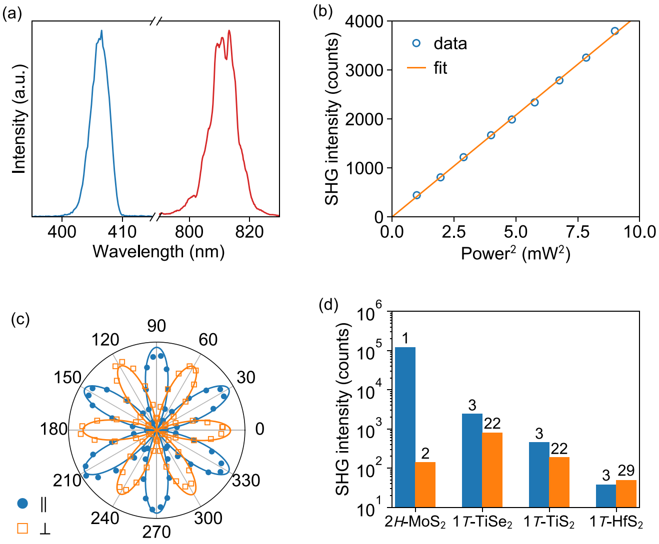

FIG. 3. (a) Spectrum showing the fundamental excitation centered at 810 nm and the SHG at 405 nm. (b) Power dependence of the SHG intensity, showing a quadratic relation. (c) Polarization dependence of the SHG in trilayer TiSe$_2$ at 4 K. The filled and open symbols represent data collected in the collinear and cross polarization configurations, respectively. The solid lines are fits to $\sin^2(3\theta)$ and $\cos^2(3\theta)$. (d) SHG intensity for 2H-MoS$_2$, 1T-TiSe$_2$, 1T-TiS$_2$, and 1T-HfS$_2$ under equivalent experimental conditions. Layer numbers are specified on top of the bars.

Figure 4(b) shows the spatial mapping of the SHG intensity of an exfoliated TiSe$_2$ sample. The corresponding optical image is shown in Fig. 4(a), with the layer numbers labeled, and a larger-scale image is included in Supplemental Material Fig. S2 [54]. Clear thickness dependence is observed, which is quantified in Fig. 4(c). The maximum in the trilayer was reproduced in multiple samples (see Supplemental Material Fig. S3 [54]). Because the whole flake derives from the same crystal, polarization-dependent measurements show that regions of different thickness exhibit the same orientation [see inset to Fig. 4(c)]. Figure 4(d) shows the temperature dependence of the SHG. It monotonically decreases by about 40% from 4 to 300 K and shows no clear signature of the CDW transition, regardless of the sample thickness.

IV. ORIGIN FOR THE SHG

The observation of strong SHG in TiSe$_2$ is unexpected given the centrosymmetric structure of the typical octohedral 1T coordination. Because of the normal-incidence measurement configuration, the electric-quadrupole contribution is unlikely to dominate [55]. The clear thickness dependence of the SHG suggests its dominant contribution from the bulk rather than from the surface. One possibility is that the TiSe$_6$ octrahedra are distorted, as typically found in the distorted octahedral coordination. Indeed, SHG has been observed in 1T'-MoTe$_2$ [56,57], 1T'-ReS$_2$ [58], and T_d-WTe$_2$ [59]. However, the SHG for these materials only appears in even-layer samples and shows twofold polarization dependence. In fact, if such distortions were present, the space group of the normal phase should have been entirely different, giving rise to characteristic Raman-active phonon modes [56]. Our observation of just the E_g and A_{1g} phonons at 300 K for the D_{3d}^3 space group rules out this possibility. This leaves the CDW-related lattice distortion as a natural explanation for the SHG. At first glance, this conclusion seems at odds with the persistence of SHG above T_{CDW}. However, at room temperature, electron and x-ray diffraction on bulk samples revealed diffuse scattering showing the CDW superlattice periodicity [60], x-ray scattering found CDW correlation [61], and angle resolved photoemission spectroscopy measurements showed gap opening [14,26,62], all attributed to local fluctuations into the CDW superlattice. More strikingly, scanning tunneling microscopy study at room temperature revealed disconnected but highly oriented triangular structures occupying a sizable fraction of the lattice [63], with their possible origin related to excess Ti atoms [64], which induce Jahn-Teller distortion [9,65] and act as nucleation centers for the CDW [66]. The observation of the SHG above T_{CDW} could be another indication for the strong fluctuation effects, in the sense that the system is unstable in the normal phase, with a tendency to lower its energy by locally distorting the lattice. The locally distorted clusters still lock to the pristine lattice, explaining the same polarization dependence as that in the coherently ordered low-temperature phase, shown in the inset to Fig. 4(d).

The sixfold polarization dependence is compatible with the established superlattice pattern for TiSe$_2$ shown in Fig. 1(b). In those octahedra where the Ti atoms remain undisplaced, the Se atoms in the planes above and below the central Ti plane rotate in opposite directions, with a tendency to transform to the trigonal prismatic coordination seen in the 2H-type transition metal dichalcogenides. This forms the basis of the band Jahn-Teller effect that was thought to drive the CDW formation in TiSe$_2$ [9]. Such distortion, as shown in Fig. 1(a) breaks the inversion symmetry and induces SHG. Moreover, an in-plane threefold rotational symmetry of the distorted lattice can be identified, with the rotation axis going through any atom that remains undisplaced. For samples thicker than one monolayer, the superlattice features a $2c_0$ periodicity along the c axis [8,10,50]. First-principles calculations confirm that the system is indeed more stable when the two adjacent distorted monolayers are stacked out of phase [67]. This stacking order restores the inversion symmetry in the bilayer, with the inversion center situated midway in the van der Waals gap, and should eliminate SHG, similar to that in 2H-MoS$_2$ [42]. However, TiSe$_2$ is highly absorbing in the optical and infrared frequency range [13]. As we show below, this can cause incomplete cancellation of the contributions from the constituent monolayers and hence SHG remains finite.

The thickness dependence shown in Fig. 4(c) can be understood along this line. Assuming each monolayer contributes a nonlinear dipole $P_{2\omega}^j = \chi^{(2)}E^2(\omega)$ and considering antiparallel stacking for the CDW phase, the components in all N layers superimpose to yield the total SHG intensity $I_{2\omega} = |\sum_{j=1}^N P_{2\omega}^j e^{i\phi_j}|^2$, with ϕ_j alternating between 0 and π. Taking into account finite absorption when the fundamental and second-harmonic electromagnetic waves propagate through the material, one can qualitatively explain the nonmonotonic thickness dependence for samples thinner than tetralayer and

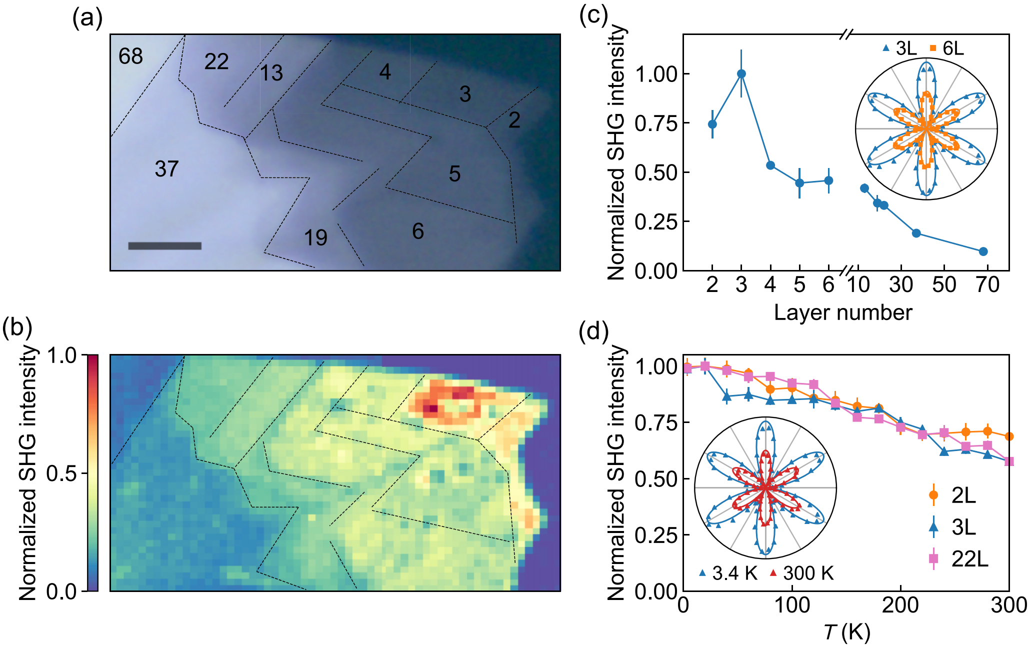

FIG. 4. (a) Optical image of exfoliated TiSe$_2$ with layer numbers labeled. Scale bar: 5 μm. (b) SHG intensity map for the sample in (a) measured at 4 K in the cross polarization configuration. (c) Thickness dependence of the SHG intensity, corresponding to the statistical average of the signal in different regions in (b). Error bars are standard deviations from the statistical analysis. The inset shows the polarization dependence measured in the trilayer and 6-layer regions. (d) Temperature dependence of the SHG intensity for bilayer, trilayer, and 22-layer TiSe$_2$, normalized to the corresponding value at 4 K. Error bars are derived from repeated measurements. The inset shows the polarization dependence for the trilayer sample at 4 K and 300 K.

the flattening out for pentalayer and thicker (see Supplemental Material Note 2 [54]). This is also consistent with the same polarization dependence for samples of different thickness, shown in the inset to Fig. 4(c), because a phase shift of π between adjacent layers does not alter the angular dependence.

Intriguingly, appreciable SHG was also observed in 1T-TiS$_2$, as shown in Fig. 3(d). This is consistent with the observation of diffuse streaking in bulk 1T-TiS$_2$ from electron diffraction [68]—which was also attributed to the Jahn-Teller distortion mechanism—and with the suggestion that 1T-TiS$_2$ exhibits incipient CDW [69]. We found that its SHG is independent of temperature and its Raman spectra do not show new modes upon cooling (see Supplemental Material Fig. S4 [54]), signifying the absence of a CDW transition. The isostructural 1T-HfS$_2$ exhibits temperature-independent SHG as well (see Supplemental Material Fig. S5 [54]), albeit with a signal almost one order of magnitude weaker than in 1T-TiS$_2$ [Fig. 3(d)]. This is in line with the electronic stability of 1T-HfS$_2$, as it is a semiconductor with a band gap over 1 eV [70].

To further elucidate the relation between the lattice distortion and the CDW transition, we have calculated from first-principles the electronic and vibrational properties of bulk and monolayer TiSe$_2$ as two thickness extremes of this system, using the superlattice proposed by Di Salvo *et al.* [8] shown Fig. 1(b). The bulk (monolayer) results are shown in Fig. 5 (Supplemental Material Note 3 [54]). These results strongly support the Jahn-Teller mechanism as the driving force for the CDW in TiSe$_2$ [9]. A characteristic feature of this mechanism is the distortion of the otherwise isotropically coordinated metal-ligand bonds [see Fig. 1(a)], thereby enhancing charge transfer from the metal to ligand, and hence, the overall stability of the whole structure. The superlattice considered in our calculations similarly distorts the octahedrally coordinated Ti-Se bonds, creating new channels to transfer charge from Ti-3d orbitals to Se-4p orbitals, hence pushing the resulting bonding to a semi-ionic d^0 state. The manifestation of this mechanical distortion is a deprivation of electronic states at the Fermi level, turning into a CDW-like band gap at sufficiently large distortions, as shown in Figs. 5(b)–5(d) and Supplemental Material Note 3 [54].

The fingerprint of this geometrical reformation can also be seen in the vibrational modes. In the absence of any distortion, TiSe$_2$ suffers from negative phonon frequencies at its Brillouin zone's boundary center, M, regardless of its thickness, as shown in Fig. 5(e) and Supplemental Material Note 3 [54]. This is a symptom of structural instability existing in this system. Remarkably, even a tiny bit of the proposed distortion removes all these negative frequencies, hinting at how CDW prevails in this system. To confirm this further, we have also calculated the Raman and infrared spectra for both bulk and monolayer TiSe$_2$ [see Fig. 5(e) and Supplemental Material Note 3 [54]]. Comparing the calculated Raman peaks with that in Fig. 1(f) reveals excellent agreement in terms of both frequency and relative intensity of the A_{1g} and E_g modes. For distorted structures, we have only calculated the infrared spectra, as they are more computationally affordable. Nevertheless, this should not be an issue, as we are interested in the frequency region where CDW peaks appear. Remarkably, once the distortion is introduced, no matter how small, additional peaks clustering around the E_u mode emerge. The frequency region of these peaks is consistent with that reported in previous infrared

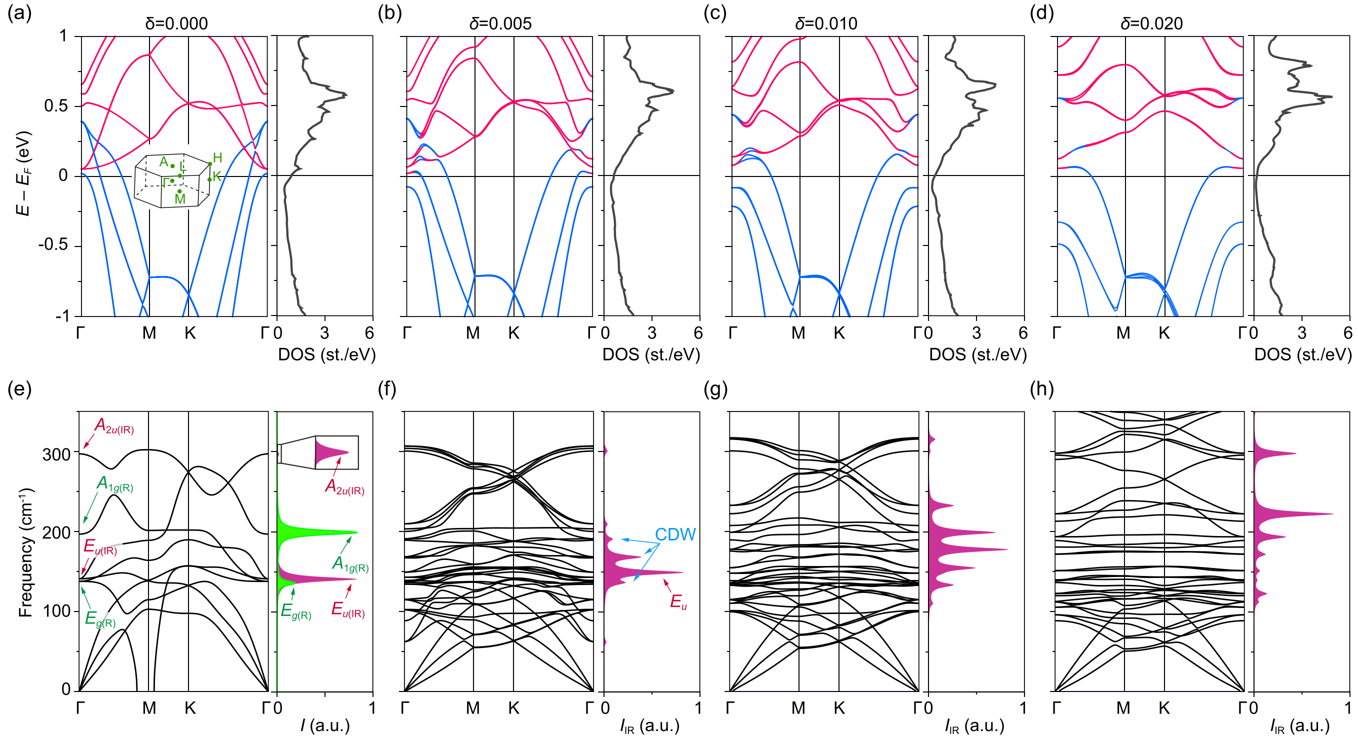

FIG. 5. Electronic band structure and density of states (DOS) of (a) bulk 1T-TiSe$_2$ and (b)–(d) its CDW phase. Above, δ corresponds to the bond length distortion ratio according to the superlattice pattern illustrated in Fig. 1(b). Upon increasing δ, the band structure undergoes significant reconstruction, developing a CDW-like gap around the Fermi level. Blue color corresponds to Se-based bands and red indicates the Ti-dominated bands. The corresponding phonon structure and infrared (IR) spectra are shown in (e)–(h). We have also included the Raman (R) spectra for the pristine lattice to compare the Raman-active phonon modes with the IR ones.

experiments [13,50,68]. This reassures the planar nature of the CDW distortions observed in this system and, more importantly, reveals that TiSe$_2$ is, in general, an inversion-asymmetric system even though marginally at ambient conditions.

Overall, these calculations combined with the observation of SHG suggest that lattice distortion is already present in TiSe$_2$ even at room temperature but perhaps not sufficient to form a collective response, observable as a CDW transition. Cooling the sample is expected to enhance the lattice distortion monotonically to the extent that below a certain critical temperature ($\sim$200 K according to our experiments), the system can exhibit a clear CDW transition with a (partial) gap opening at the Fermi level. As SHG can more sensitively probe the local distortions, it can thus reveal such microscopic features before they become strong enough to appear in Raman measurements. The slow variation of SHG below T_{CDW} is due to the fact that by the time the system exhibits its collective response to the cooling in the form of the CDW phase transition, it has already undergone substantial local distortions. As such, further cooling can only slightly affect the local displacements and their optical implications, appearing as a slow linear evolution of SHG at low temperatures shown in Fig. 4(d).

V. DISCUSSION

Having established the CDW origin of the SHG, we now discuss the possibility of the chiral CDW phase in TiSe$_2$. The proposal of the chiral CDW [35,36] builds upon the triple-q CDW state, with phase shift between the CDW wave vectors. One of the three components lies within the monolayer while the other two reside in virtual layers in the van der Waals gap. This is expected to break the inversion symmetry, but the associated point group is C_2 [37], in contradiction with the threefold rotational symmetry suggested by our data. Recent STM [38], x-ray natural circular dichroism [39], and x-ray diffraction [40] results as well as reinterpretation [41] of previous x-ray diffraction data [36] also suggest that the CDW is achiral. A recent work reported evidence of a stimulus-induced chiral order in TiSe$_2$ by shining circularly polarized light on the sample while it was cooled from above T_{CDW} to 50 K [71]. Whether this order is associated with a chiral CDW phase could be checked by performing polarization-resolved SHG on the light-trained samples, to see if it is compatible with the C_2 symmetry.

The thickness dependence of T_{CDW} observed here bears important implications for the CDW mechanism. The samples were encapsulated to minimize degradation, and the insulating sapphire substrate is expected to interact weakly with them, hence the dimensionality effect found in our work should be intrinsic. 2D semiconductors in the transition metal dichalcogenide family have been shown to exhibit prominent excitonic effects, due to the combination of spatial confinement and the enhanced Coulomb interactions resulting from reduced dielectric screening [72]. Analogously, excitonic effects should be more pronounced in atomically thin TiSe$_2$ than in its bulk counterpart. Our observation of the weak dimensionality effect on T_{CDW} and the indication that T_{CDW} is even reduced in the 2D limit challenges the exciton insulator scenario, although this is widely believed to drive the CDW formation in TiSe_2 [14,15,18,19].

VI. CONCLUSION

To summarize, we have observed SHG in TiSe_2 from bulk to atomically thin layers, which can be ascribed to the lattice distortion induced by the CDW formation in this system. Combined with Raman spectroscopy of the CDW phase, the polarization and thickness dependence of the SHG suggest that the superlattice pattern, particularly its $2c_0$ periodicity along the c axis, remains unchanged down to two monolayers. Our work suggests broken inversion symmetry in the constituent monolayers of TiSe_2 in its CDW phase, which may have interesting consequences on the coexisting superconducting state under certain conditions.

ACKNOWLEDGMENTS

This work was supported by the National Key Research and Development Program of China (Grants No. 2018YFA0307000 and No. 2017YFA0303201), the National Natural Science Foundation of China (Grants No. 11774151 and No. 51972163), and Fundamental Research Funds for the Central Universities (Grant No. 020414380147). The work in Lausanne was supported by the Swiss National Science Foundation. Growth of hexagonal boron nitride crystals was supported by the Elemental Strategy Initiative conducted by the MEXT, Japan (Grant No. JPMXP0112101001), JSPS KAKENHI (Grant No. JP20H00354), and A3 Foresight by JSPS. A.R., R.V.B., and M.S.B. gratefully acknowledge the Center for Computational Materials Science in the Institute for Materials Research for allocations on the MASAMUNE-IMR supercomputer system (Project No. 20S0512). A.R. and T.K. are thankful to the Paderborn Center for Parallel Computing (PC2) for offering computing time on OCuLUS and the FPGA-based supercomputer NOCTUA.

APPENDIX: METHODS

1. Sample preparation

TiSe_2 single crystals were grown by the chemical vapor transport method. Atomically thin samples were produced by mechanical exfoliation and transferred on sapphire substrates, carried out in a glovebox filled with N_2 gas. The flakes were encapsulated by h-BN with 10–20 nm thickness before being exposed to air. Although monolayer samples are in principle achievable, the thinnest samples we obtained were bilayers, due to the low yield and small lateral size of the monolayers. The flake thickness was determined by the layer-number dependent Raman modes if thinner than six layers and by atomic force microscopy for thicker samples. $2H$-MoS_2, $1T$-TiS_2, and $1T$-HfS_2 crystals were purchased from SixCarbon Technology Shenzhen.

2. Raman and SHG characterizations

Raman scattering spectroscopy and SHG were performed using a home-built confocal microscopy setup under normal incidence with a 40× microscope objective. Raman scattering was performed using 633 nm laser excitation and a power of 0.15–0.40 mW. The backscattered signal passed through notch filters and was detected using a spectrometer and a CCD detector. SHG was performed using a Ti:sapphire oscillator, with the fundamental excitation set to 810 nm, pulse width of 70 fs, and repetition rate of 80 MHz. The SHG spectra were checked using the aforementioned spectrometer, but for systematic polarization- and temperature-dependent studies the signal was detected using a photomultiplier tube, with a bandpass filter positioned before the detectors to single out the second-harmonic signal. Spatial mapping was achieved using a dual-axis scanning galvo system. The polarization direction of the incident beam was varied using a polarizer and a half-wave plate, while another polarizer in the detection path set the collinear or cross polarization configurations. Samples were placed in a vacuum cryostat throughout the measurement.

3. First-principles calculations

The electronic structure calculations were performed within density functional theory using Perdew-Burke-Ernzerhof exchange-correlation functional [73] and projector augmented wave method as implemented in the VASP program [74,75]. We considered a $2 \times 2 \times 1$ superlattice derived from the unit cell of $1T$-TiSe_2 and manually distorted it using the pattern proposed in Ref. [8]. The corresponding Brillouin zone was sampled using a $8 \times 8 \times 8$ ($8 \times 8 \times 1$) k mesh for the bulk (monolayer) superlattice. The plane-wave cutoff energy was set to 520 eV, and the total energy convergence was fixed at 10^{-8} eV. Relativistic corrections, including spin-orbit interaction, were fully taken into account. The vibrational properties were determined using PHONO3PYcode [76] interfaced with VASP. For this, we first expanded each bulk (monolayer) superlattice into a $2 \times 2 \times 2$ ($2 \times 2 \times 1$) supercell, then computed the real space force constants up to third order using the finite displacement method implemented in VASP, and finally, fed them into PHONO3PY and PHONON-SPECTROSCOPY [77] to calculate the phonon modes and their resulting Raman and infrared spectra.

In our calculations to consider the CDW instability of the pristine structures at high temperatures, we took a realistic thermal broadening factor of $\sigma = 0.05$ eV for the Fermi-Dirac smearing method used to sample the partially occupied states at the Fermi level. This enforced imaginary phonon frequencies centered at the M point in the Brillouin zone (BZ). We emphasize that the choice of this σ value was intentional, as it enabled us to examine whether introducing the proposed structural distortion can dynamically stabilize the whole structure (and thus remove the imaginary frequencies) or destabilize it. It is worth noting that increasing σ can artificially vanish the imaginary frequencies at the M point [53,78]. Nevertheless, at the BZ center Γ point, which is relevant for Raman spectra analysis, the σ variation has a marginal effect and is therefore negligible (see Supplemental Material Note 4 [54]).

[1] Y. Cao, V. Fatemi, A. Demir, S. Fang, S. L. Tomarken, J. Y. Luo, J. D. Sanchez-Yamagishi, K. Watanabe, T. Taniguchi, E. Kaxiras, R. C. Ashoori, and P. Jarillo-Herrero, Nature (London) **556**, 80 (2018).

[2] Y. Cao, V. Fatemi, S. Fang, K. Watanabe, T. Taniguchi, E. Kaxiras, and P. Jarillo-Herrero, Nature (London) **556**, 43 (2018).

[3] N. Sivadas, S. Okamoto, X. Xu, C. J. Fennie, and D. Xiao, Nano Lett. **18**, 7658 (2018).

[4] W. Chen, Z. Sun, Z. Wang, L. Gu, X. Xu, S. Wu, and C. Gao, Science **366**, 983 (2019).

[5] G. H. Han, D. L. Duong, D. H. Keum, S. J. Yun, and Y. H. Lee, Chem. Rev. **118**, 6297 (2018).

[6] T. Ritschel, H. Berger, and J. Geck, Phys. Rev. B **98**, 195134 (2018).

[7] S.-H. Lee, J. S. Goh, and D. Cho, Phys. Rev. Lett. **122**, 106404 (2019).

[8] F. J. Di Salvo, D. E. Moncton, and J. V. Waszczak, Phys. Rev. B **14**, 4321 (1976).

[9] H. P. Hughes, J. Phys. C: Solid State Phys. **10**, L319 (1977).

[10] J. A. Wilson, Phys. Status Solidi B **86**, 11 (1978).

[11] T. E. Kidd, T. Miller, M. Y. Chou, and T. C. Chiang, Phys. Rev. Lett. **88**, 226402 (2002).

[12] K. Rossnagel, L. Kipp, and M. Skibowski, Phys. Rev. B **65**, 235101 (2002).

[13] G. Li, W. Z. Hu, D. Qian, D. Hsieh, M. Z. Hasan, E. Morosan, R. J. Cava, and N. L. Wang, Phys. Rev. Lett. **99**, 027404 (2007).

[14] H. Cercellier, C. Monney, F. Clerc, C. Battaglia, L. Despont, M. G. Garnier, H. Beck, P. Aebi, L. Patthey, H. Berger, and L. Forró, Phys. Rev. Lett. **99**, 146403 (2007).

[15] J. van Wezel, P. Nahai-Williamson, and S. S. Saxena, Phys. Rev. B **81**, 165109 (2010).

[16] F. Weber, S. Rosenkranz, J.-P. Castellan, R. Osborn, G. Karapetrov, R. Hott, R. Heid, K.-P. Bohnen, and A. Alatas, Phys. Rev. Lett. **107**, 266401 (2011).

[17] M. Calandra and F. Mauri, Phys. Rev. Lett. **106**, 196406 (2011).

[18] A. Kogar, M. S. Rak, S. Vig, A. A. Husain, F. Flicker, Y. I. Joe, L. Venema, G. J. MacDougall, T. C. Chiang, E. Fradkin, J. van Wezel, and P. Abbamonte, Science **358**, 1314 (2017).

[19] T. Kaneko, Y. Ohta, and S. Yunoki, Phys. Rev. B **97**, 155131 (2018).

[20] E. Morosan, H. W. Zandbergen, B. S. Dennis, J. W. G. Bos, Y. Onose, T. Klimczuk, A. P. Ramirez, N. P. Ong, and R. J. Cava, Nat. Phys. **2**, 544 (2006).

[21] A. F. Kusmartseva, B. Sipos, H. Berger, L. Forró, and E. Tutiš, Phys. Rev. Lett. **103**, 236401 (2009).

[22] L. J. Li, E. C. T. O'Farrell, K. P. Loh, G. Eda, B. Özyilmaz, and A. H. Castro Neto, Nature (London) **529**, 185 (2016).

[23] P. Goli, J. Khan, D. Wickramaratne, R. K. Lake, and A. A. Balandin, Nano Lett. **12**, 5941 (2012).

[24] D. L. Duong, G. Ryu, A. Hoyer, C. Lin, M. Burghard, and K. Kern, ACS Nano **11**, 1034 (2017).

[25] J. Li, P. Song, J. Zhao, K. Vaklinova, X. Zhao, Z. Li, Z. Qiu, Z. Wang, L. Lin, M. Zhao, T. S. Herng, Y. Zuo, W. Jonhson, W. Yu, X. Hai, P. Lyu, H. Xu, H. Yang, C. Chen, S. J. Pennycook *et al.*, Nat. Mater. **20**, 181 (2021).

[26] P. Chen, Y. H. Chan, X. Y. Fang, Y. Zhang, M. Y. Chou, S. K. Mo, Z. Hussain, A. V. Fedorov, and T. C. Chiang, Nat. Commun. **6**, 8943 (2015).

[27] J.-P. Peng, J.-Q. Guan, H.-M. Zhang, C.-L. Song, L. Wang, K. He, Q.-K. Xue, and X.-C. Ma, Phys. Rev. B **91**, 121113(R) (2015).

[28] P. Chen, Y. H. Chan, M. H. Wong, X. Y. Fang, M. Y. Chou, S. K. Mo, Z. Hussain, A. V. Fedorov, and T. C. Chiang, Nano Lett. **16**, 6331 (2016).

[29] K. Sugawara, Y. Nakata, R. Shimizu, P. Han, T. Hitosugi, T. Sato, and T. Takahashi, ACS Nano **10**, 1341 (2016).

[30] S. Kolekar, M. Bonilla, Y. Ma, H. C. Diaz, and M. Batzill, 2D Mater. **5**, 015006 (2017).

[31] J. Wang, H. Zheng, G. Xu, L. Sun, D. Hu, Z. Lu, L. Liu, J. Zheng, C. Tao, and L. Jiao, J. Am. Chem. Soc. **138**, 16216 (2016).

[32] W. Hong, C. Yu, D. Martial, Z. Qingsheng, W. Xuewen, T. S. Hon, L. Hongling, J. Lin, Y. Ting, T. E. H. Tong, and L. Zheng, Adv. Mater. **30**, 1704382 (2018).

[33] H. Lin, Q. Zhu, D. Shu, D. Lin, J. Xu, X. Huang, W. Shi, X. Xi, J. Wang, and L. Gao, Nat. Mater. **18**, 602 (2019).

[34] R. Ganesh, G. Baskaran, J. van den Brink, and D. V. Efremov, Phys. Rev. Lett. **113**, 177001 (2014).

[35] J. Ishioka, Y. H. Liu, K. Shimatake, T. Kurosawa, K. Ichimura, Y. Toda, M. Oda, and S. Tanda, Phys. Rev. Lett. **105**, 176401 (2010).

[36] J.-P. Castellan, S. Rosenkranz, R. Osborn, Q. Li, K. E. Gray, X. Luo, U. Welp, G. Karapetrov, J. P. C. Ruff, and J. van Wezel, Phys. Rev. Lett. **110**, 196404 (2013).

[37] M. Gradhand and J. van Wezel, Phys. Rev. B **92**, 041111(R) (2015).

[38] B. Hildebrand, T. Jaouen, M. L. Mottas, G. Monney, C. Barreteau, E. Giannini, D. R. Bowler, and P. Aebi, Phys. Rev. Lett. **120**, 136404 (2018).

[39] C. W. Chuang, Y. Tanaka, M. Oura, K. Rossnagel, and A. Chainani, Phys. Rev. B **102**, 195102 (2020).

[40] H. Ueda, M. Porer, J. R. L. Mardegan, S. Parchenko, N. Gurung, F. Fabrizi, M. Ramakrishnan, L. Boie, M. J. Neugebauer, B. Burganov, M. Burian, S. L. Johnson, K. Rossnagel, and U. Staub, Phys. Rev. Res. **3**, L022003 (2021).

[41] M.-K. Lin, J. A. Hlevyack, P. Chen, R.-Y. Liu, and T.-C. Chiang, Phys. Rev. Lett. **122**, 229701 (2019).

[42] Y. L. Li, Y. Rao, K. F. Mak, Y. M. You, S. Y. Wang, C. R. Dean, and T. F. Heinz, Nano Lett. **13**, 3329 (2013).

[43] N. Kumar, S. Najmaei, Q. Cui, F. Ceballos, P. M. Ajayan, J. Lou, and H. Zhao, Phys. Rev. B **87**, 161403(R) (2013).

[44] L. M. Malard, T. V. Alencar, Ana Paula M. Barboza, K. F. Mak, and A. M. de Paula, Phys. Rev. B **87**, 201401(R) (2013).

[45] H. Zeng, G.-B. Liu, J. Dai, Y. Yan, B. Zhu, R. He, L. Xie, S. Xu, X. Chen, W. Yao, and X. Cui, Sci. Rep. **3**, 1608 (2013).

[46] J. Shi, P. Yu, F. Liu, P. He, R. Wang, L. Qin, J. Zhou, X. Li, J. Zhou, X. Sui, S. Zhang, Y. Zhang, Q. Zhang, T. C. Sum, X. Qiu, Z. Liu, and X. Liu, Adv. Mater. **29**, 1701486 (2017).

[47] Z. Sun, Y. Yi, T. Song, G. Clark, B. Huang, Y. Shan, S. Wu, D. Huang, C. Gao, Z. Chen, M. McGuire, T. Cao, D. Xiao, W.-T. Liu, W. Yao, X. Xu, and S. Wu, Nature (London) **572**, 497 (2019).

[48] J. Xiao, H. Zhu, Y. Wang, W. Feng, Y. Hu, A. Dasgupta, Y. Han, Y. Wang, D. A. Muller, L. W. Martin, P. A. Hu, and X. Zhang, Phys. Rev. Lett. **120**, 227601 (2018).

[49] F. Xue, W. Hu, K.-C. Lee, L.-S. Lu, J. Zhang, H.-L. Tang, A. Han, W.-T. Hsu, S. Tu, W.-H. Chang, C.-H. Lien, J.-H. He, Z.

Zhang, L.-J. Li, and X. Zhang, Adv. Funct. Mater. **28**, 1803738 (2018).

[50] J. A. Holy, K. C. Woo, M. V. Klein, and F. C. Brown, Phys. Rev. B **16**, 3628 (1977).

[51] C. S. Snow, J. F. Karpus, S. L. Cooper, T. E. Kidd, and T. C. Chiang, Phys. Rev. Lett. **91**, 136402 (2003).

[52] H. Barath, M. Kim, J. F. Karpus, S. L. Cooper, P. Abbamonte, E. Fradkin, E. Morosan, and R. J. Cava, Phys. Rev. Lett. **100**, 106402 (2008).

[53] D. Lin, S. Li, J. Wen, H. Berger, L. Forró, H. Zhou, S. Jia, T. Taniguchi, K. Watanabe, X. Xi, and M. S. Bahramy, Nat. Commun. **11**, 2406 (2020).

[54] See Supplemental Material at http://link.aps.org/supplemental/10.1103/PhysRevB.105.085409 for methods of data analysis and more supporting data.

[55] Y. Zhang, D. Huang, Y. Shan, T. Jiang, Z. Zhang, K. Liu, L. Shi, J. Cheng, J. E. Sipe, W.-T. Liu, and S. Wu, Phys. Rev. Lett. **122**, 047401 (2019).

[56] R. Beams, L. G. Cançado, S. Krylyuk, I. Kalish, B. Kalanyan, A. K. Singh, K. Choudhary, A. Bruma, P. M. Vora, F. Tavazza, A. V. Davydov, and S. J. Stranick, ACS Nano **10**, 9626 (2016).

[57] Y. Wang, J. Xiao, H. Zhu, Y. Li, Y. Alsaid, K. Y. Fong, Y. Zhou, S. Wang, W. Shi, Y. Wang, A. Zettl, E. J. Reed, and X. Zhang, Nature (London) **550**, 487 (2017).

[58] Y. Song, S. Hu, M.-L. Lin, X. Gan, P.-H. Tan, and J. Zhao, ACS Photonics **5**, 3485 (2018).

[59] E. J. Sie, C. M. Nyby, C. D. Pemmaraju, S. J. Park, X. Shen, J. Yang, M. C. Hoffmann, B. K. Ofori-Okai, R. Li, A. H. Reid, S. Weathersby, E. Mannebach, N. Finney, D. Rhodes, D. Chenet, A. Antony, L. Balicas, J. Hone, T. P. Devereaux, T. F. Heinz *et al.*, Nature (London) **565**, 61 (2019).

[60] K. C. Woo, F. C. Brown, W. L. McMillan, R. J. Miller, M. J. Schaffman, and M. P. Sears, Phys. Rev. B **14**, 3242 (1976).

[61] Y. I. Joe, X. M. Chen, P. Ghaemi, K. D. Finkelstein, G. A. de la Pena, Y. Gan, J. C. T. Lee, S. Yuan, J. Geck, G. J. MacDougall, T. C. Chiang, S. L. Cooper, E. Fradkin, and P. Abbamonte, Nat. Phys. **10**, 421 (2014).

[62] C. Monney, E. F. Schwier, M. G. Garnier, N. Mariotti, C. Didiot, H. Beck, P. Aebi, H. Cercellier, J. Marcus, C. Battaglia, H. Berger, and A. N. Titov, Phys. Rev. B **81**, 155104 (2010).

[63] M. V. Kuznetsov, I. Ogorodnikov, A. S. Vorokh, A. S. Rasinkin, and A. N. Titov, Surf. Sci. **606**, 1760 (2012).

[64] B. Hildebrand, C. Didiot, A. M. Novello, G. Monney, A. Scarfato, A. Ubaldini, H. Berger, D. R. Bowler, C. Renner, and P. Aebi, Phys. Rev. Lett. **112**, 197001 (2014).

[65] B. Hildebrand, T. Jaouen, C. Didiot, E. Razzoli, G. Monney, M.-L. Mottas, F. Vanini, C. Barreteau, A. Ubaldini, E. Giannini, H. Berger, D. R. Bowler, and P. Aebi, Phys. Rev. B **95**, 081104(R) (2017).

[66] B. Hildebrand, T. Jaouen, C. Didiot, E. Razzoli, G. Monney, M.-L. Mottas, A. Ubaldini, H. Berger, C. Barreteau, H. Beck, D. R. Bowler, and P. Aebi, Phys. Rev. B **93**, 125140 (2016).

[67] R. Bianco, M. Calandra, and F. Mauri, Phys. Rev. B **92**, 094107 (2015).

[68] F. C. Brown, Phys. B+C **99**, 264 (1980).

[69] K. Dolui and S. Sanvito, Europhys. Lett. **115**, 47001 (2016).

[70] T. Kanazawa, T. Amemiya, A. Ishikawa, V. Upadhyaya, K. Tsuruta, T. Tanaka, and Y. Miyamoto, Sci. Rep. **6**, 22277 (2016).

[71] S.-Y. Xu, Q. Ma, Y. Gao, A. Kogar, A. Zong, A. M. Mier Valdivia, T. H. Dinh, S.-M. Huang, B. Singh, C.-H. Hsu, T.-R. Chang, J. P. C. Ruff, K. Watanabe, T. Taniguchi, H. Lin, G. Karapetrov, D. Xiao, P. Jarillo-Herrero, and N. Gedik, Nature (London) **578**, 545 (2020).

[72] A. Chernikov, T. C. Berkelbach, H. M. Hill, A. Rigosi, Y. Li, O. B. Aslan, D. R. Reichman, M. S. Hybertsen, and T. F. Heinz, Phys. Rev. Lett. **113**, 076802 (2014).

[73] J. P. Perdew, K. Burke, and M. Ernzerhof, Phys. Rev. Lett. **77**, 3865 (1996).

[74] G. Kresse and J. Furthmüller, Phys. Rev. B **54**, 11169 (1996).

[75] G. Kresse and D. Joubert, Phys. Rev. B **59**, 1758 (1999).

[76] A. Togo, L. Chaput, and I. Tanaka, Phys. Rev. B **91**, 094306 (2015).

[77] J. M. Skelton, L. A. Burton, A. J. Jackson, F. Oba, S. C. Parker, and A. Walsh, Phys. Chem. Chem. Phys. **19**, 12452 (2017).

[78] D. L. Duong, M. Burghard, and J. C. Schön, Phys. Rev. B **92**, 245131 (2015).